J. Fluid Mech. (2013), *vol.* 736, *pp.* 177–194.
doi:10.1017/jfm.2013.488

Comparison between two- and three-dimensional Rayleigh–Bénard convection

Erwin P. van der Poel[1],†, Richard J. A. M. Stevens[1,2] and Detlef Lohse[1]

[1]Department of Science and Technology and J.M. Burgers Center for Fluid Dynamics, University of Twente, P.O Box 217, 7500 AE Enschede, The Netherlands

[2]Department of Mechanical Engineering, Johns Hopkins University, Baltimore, Maryland 21218, USA

(Received 28 March 2013; revised 5 September 2013; accepted 11 September 2013; first published online 4 November 2013)

Two-dimensional and three-dimensional Rayleigh–Bénard convection is compared using results from direct numerical simulations and previous experiments. The phase diagrams for both cases are reviewed. The differences and similarities between two- and three-dimensional convection are studied using $Nu(Ra)$ for $Pr = 4.38$ and $Pr = 0.7$ and $Nu(Pr)$ for Ra up to 10^8. In the $Nu(Ra)$ scaling at higher Pr, two- and three-dimensional convection is very similar, differing only by a constant factor up to $Ra = 10^{10}$. In contrast, the difference is large at lower Pr, due to the strong roll state dependence of Nu in two dimensions. The behaviour of $Nu(Pr)$ is similar in two and three dimensions at large Pr. However, it differs significantly around $Pr = 1$. The Reynolds number values are consistently higher in two dimensions and additionally converge at large Pr. Finally, the thermal boundary layer profiles are compared in two and three dimensions.

Key words: Bénard convection, turbulent flows, turbulent convection

1. Introduction

In Rayleigh–Bénard (RB) convection a fluid in a closed sample is heated from below and cooled from above. This system is widely studied due to its conceptual simplicity and because of the many applications of turbulent heat transfer, such as in geophysics, astrophysics or process technology. The control parameters of RB convection in the Boussinesq approximation are the Rayleigh number $Ra = \beta g \Delta L^3/(\kappa\nu)$, the Prandtl number $Pr = \nu/\kappa$ and the aspect ratio $\Gamma = D/L$. Here, L is the height of the sample and D its width, β is the thermal expansion coefficient, g the gravitational acceleration, Δ the temperature difference between the bottom and the top of the sample, and ν and κ the kinematic viscosity and the thermal diffusivity, respectively.

The response of the system is commonly quantified by the heat transfer and the kinetic energy, which we indicate with the Nusselt number Nu and the Reynolds number Re based on the root mean square (r.m.s.) vertical velocity, respectively:

$$Nu = \frac{\langle u_z\theta\rangle_A - \kappa\langle\partial_z\theta\rangle_A}{\kappa\Delta L^{-1}}, \tag{1.1}$$

† Email address for correspondence: e.p.vanderpoel@utwente.nl

where $\langle\cdot\rangle_A$ indicates the average over any horizontal plane (three dimensions) or line (two dimensions), and the Reynolds number Re is defined as

$$Re = \frac{u_3^{RMS} L}{\nu}, \tag{1.2}$$

where u_3^{RMS} is the r.m.s. of the vertical velocity (i.e. parallel to gravity).

Although all real-world applications of RB convection are three-dimensional (3D), two-dimensional (2D) simulations are used to better understand the physical mechanisms of 3D convection, as 2D simulations are substantially less CPU-intensive than 3D simulations. In addition, theoretical predictions for scalings in hard turbulent RB convection (Roberts 1979; Castaing *et al.* 1989; Shraiman & Siggia 1990; Grossmann & Lohse 2000, 2001, 2002, 2004, 2011) are based on 2D equations, namely the Prandtl equations for the boundary layer, or use assumptions that apply to two dimensions as well as to three. This makes it an useful tool to validate theory, regardless of the similarity between the 2D and 3D cases. Moreover, the quasi-2D character of the large-scale circulation (LSC) in both 2D and 3D flows hints at a large similarity, in particular for integral quantities, between 2D and 3D RB turbulence, in contrast to unbounded turbulence, where in three dimensions no such large-scale structures emerge.

Despite these similarities, there are significant differences between 2D and 3D convection. For example, the limited motion of the LSC in 2D convection increases the accumulation of energy in corner rolls, leading to large-scale wind reversals (Sugiyama *et al.* 2010) and high sensitivity of global output parameters on the roll state (van der Poel, Stevens & Lohse 2011). In 3D convection these phenomena are also observed by Weiss *et al.* (2010), but the additional degree of freedom of the LSC attenuates the global effects of these phenomena. Furthermore, the intrinsic inverse energy cascade (Kraichnan 1967) of 2D turbulence is fundamentally different from the forward cascade of 3D turbulence. The effect of this difference at smaller scales on global properties is unfortunately unknown. However, one can argue that for RB flows with a large-scale roll the effect must be minor, as in 3D RB the self-amplifying local driving and global temperature gradient (Ahlers, Grossmann & Lohse 2009*b*) result in a box-sized vortex, even without an inverse energy cascade. The large-scale dynamics are similar in two and three dimensions, and therefore the main difference in global output between both systems is expected to come from the small-scale dynamics.

Previous work by Schmalzl *et al.* (2004) on the validity of the 2D approach to 3D RB convection concluded that for small Pr, 2D numerics are no longer a valid representation of 3D convection, due to the increasing energy in the toroidal component of the velocity in 3D flows at lower Pr (Busse 1978). The analysis was limited to a low Rayleigh number of 10^6, which is in the laminar regime for most Pr, according to the coherence length criterion of Sugiyama *et al.* (2007). Furthermore, Schmalzl *et al.* (2004) used stress-free velocity boundary conditions on the lateral walls. Although this decreases computational requirement due to the absence of sidewall boundary layers, it complicates comparison to experiments where the boundary conditions are exhaustively no-slip. Now, eight years later, we are able to study the similarities and differences between 2D and 3D RB convection with no-slip boundary conditions at much higher Ra in the turbulent regime.

We explain the numerical methods used and provide resolution checks alongside the results. We show parameter spaces containing a comprehensive overview of available data points from 2D and 3D RB studies. A qualitative review is made using flow field snapshots of 2D and 3D flows at different Pr, illustrating the different regimes

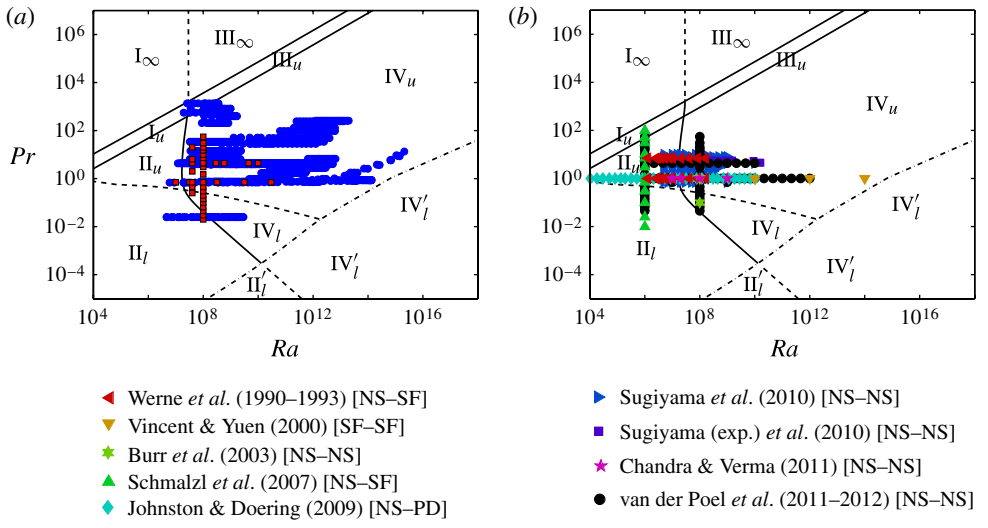

FIGURE 1. (Colour online) (*a*) Phase diagram in the *Ra–Pr* plane for 3D studies. Here simulations and experiments are indicated by red squares and blue circles respectively. For more detail and references see Stevens *et al.* (2013). (*b*) Phase diagram in the *Ra–Pr* plane for 2D studies. Note that the lines indicating the different GL regimes are taken from the 3D fit to assist the comparison of the two plots. The legend applies only to the 2D phase diagram. The data points are taken from studies where *Nu* has been measured in all aspect ratios and is from DeLuca *et al.* (1990), Werne *et al.* (1991), Werne (1993), Vincent & Yuen (2000), Burr, Kinzelbach & Tsinober (2003), Schmalzl *et al.* (2004), Johnston & Doering (2009), Sugiyama *et al.* (2010), Chandra & Verma (2011) and van der Poel *et al.* (2011) and this study. The different velocity boundary conditions used in these studies are indicated in the legend by NS (no-slip), SF (stress-free) and PD (periodic) in the format [plates–sidewalls]. Note that '(exp.)' in the legend signifies that these data are taken from quasi-2D experiments. The lines in both plots follow the GL theory (Grossmann & Lohse 2000, 2001, 2002, 2004): upper solid line, $Re = Re_c$; lower nearly parallel solid line, $\epsilon_{u,BL} = \epsilon_{u,bulk}$; curved solid line, $\epsilon_{\theta,BL} = \epsilon_{\theta,bulk}$; long-dashed line, $\lambda_u = \lambda_\theta$, i.e. $2aNu = \sqrt{Re}$. The dotted line indicates where the laminar kinetic boundary layer is expected to become turbulent, based on a critical shear Reynolds number $Re_s^* = 1014$ of the kinetic boundary layer, with $a = 0.911$ (Stevens *et al.* 2013).

in *Pr* space and their proposed effect on the 2D/3D similarity. Moreover, the thermal boundary layer profiles obtained in the 2D and 3D simulations are compared with the 'flat-plate' Pohlhausen profile.

2. Parameter space explored

We first review the explored parameter space in both experiments and numerics. Figure 1 displays the 3D and 2D phase diagrams. The lines and numbers indicate the different regimes of the Grossmann–Lohse (GL) theory based on a refit of the data (Stevens *et al.* 2013). Note that for the 2D plot the regimes resulting from the 3D fit are used. For the 3D plot, data points where *Nu* has been measured or numerically calculated have been included for aspect ratio $\Gamma = 1$ for no-slip velocity boundary conditions on all walls.

Unlike the 3D phase diagram in figure 1, multiple velocity boundary conditions are included in the 2D phase diagram, which are indicated in the legend. This increased variety in the boundary conditions employed presumably originates from the lack of 2D experiments; there is less willingness to mimic the no-slip experimental boundary conditions of experiments in 3D. In addition, the rectangular 2D geometry allows for more types of boundary conditions than the common cylindrical 3D setup, as periodic sidewalls are not possible in this case.

Comparing the two phase diagrams, it becomes clear that the 3D parameter space has been explored more, due to the availability of experiments and the closer resemblance to convection in nature. The 2D phase diagram is, apart from one experimental series, fully composed of numerical data. The highest $Ra = 10^{14}$ is obtained by Vincent & Yuen (2000) for a flow without velocity boundary layers. Evaluating the grid resolution used and the saturating $Nu(Ra)$ data, we think that this simulation is under-resolved and the heat flux was dominated by numerical diffusion. Discarding this point from the comparison and taking into account the fact that $Ra = 2 \times 10^{12}$ is the highest Rayleigh number obtained in three dimensions, it is apparent that the exploration of the parameter space in two dimensions is open for large improvement.

3. Numerical simulations

We numerically solve the three-dimensional Navier–Stokes equations within the Boussinesq approximation,

$$\frac{\mathrm{D}\boldsymbol{u}}{\mathrm{D}t} = -\boldsymbol{\nabla} P + \left(\frac{Pr}{Ra}\right)^{1/2} \nabla^2 \boldsymbol{u} + \theta \widehat{z}, \tag{3.1}$$

$$\frac{\mathrm{D}\theta}{\mathrm{D}t} = \frac{1}{(Pr\,Ra)^{1/2}} \nabla^2 \theta, \tag{3.2}$$

with $\boldsymbol{\nabla} \cdot \boldsymbol{u} = 0$. Here $\widehat{z}$ is the unit vector pointing in the opposite direction to gravity, $\mathrm{D}/\mathrm{D}t = \partial_t + \boldsymbol{u} \cdot \boldsymbol{\nabla}$ is the material derivative, $\boldsymbol{u}(\boldsymbol{x}, t)$ is the velocity vector with no-slip boundary conditions at all walls, and θ is the non-dimensional temperature, $0 \leqslant \theta \leqslant 1$. The equations have been made non-dimensional by using the length L, the temperature Δ, and the free-fall velocity $U = \sqrt{\beta g \Delta L}$. The 3D numerical scheme is described in detail in Verzicco & Orlandi (1996) and Verzicco & Camussi (1999, 2003) and the 2D scheme in Sugiyama *et al.* (2009).

For this study we performed 3D simulations at $Ra = 10^8$ and $0.02 \leqslant Pr \leqslant 0.7$ in a $\Gamma = 1$ sample and 2D simulations in a $\Gamma = 1$ sample at $Ra = 10^8$ with $0.045 \leqslant Pr \leqslant 55$, and with $Pr = 4.38$ and $10^7 \leqslant Ra \leqslant 10^{11}$ to complement some of our previous data sets (Zhong *et al.* 2009; Stevens, Clercx & Lohse 2010*a*; van der Poel *et al.* 2012).

To ensure adequate accuracy of the simulations, we compare the number of points we placed in the thermal boundary layer with the minimum number that should be placed inside the boundary layer according to Shishkina *et al.* (2010). For each Prandtl number this criterion is satisfied for the highest resolution simulation and/or checked with resolution checks. Once a simulation is properly resolved there is no dependence on the grid resolution as the grid-dependent errors diminish. This is a strict resolution criterion as it is sensitive to the resolution in the entire domain and not just in the boundary layers. Apart from the boundary layer the azimuthal resolution close to the

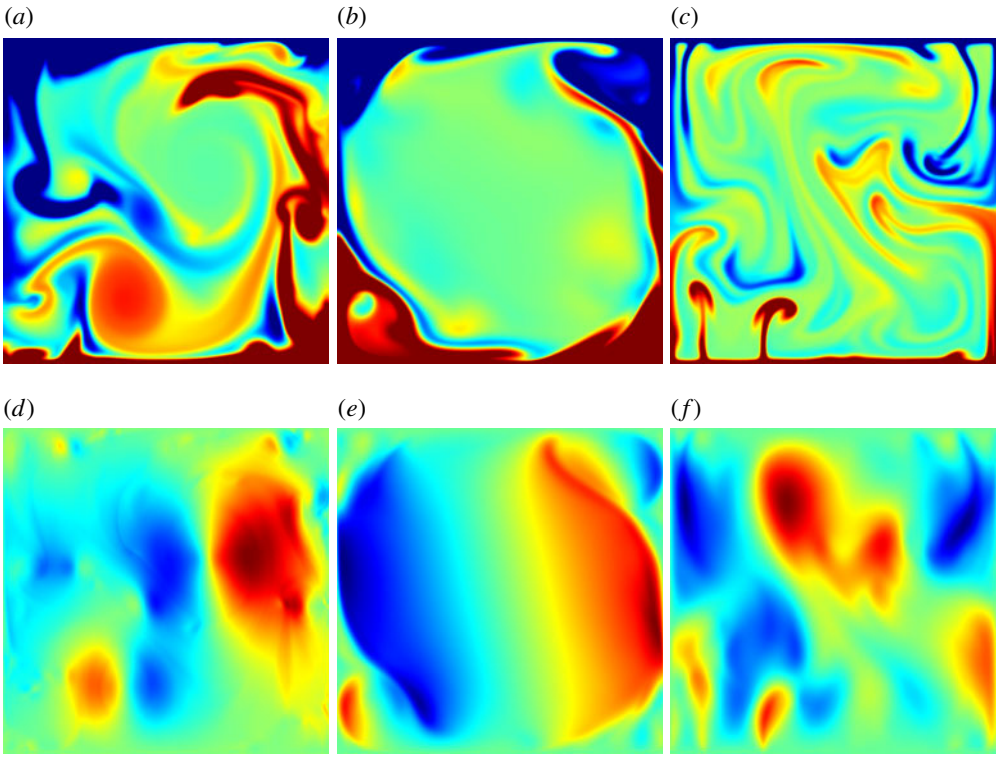

FIGURE 2. Temperature (*a–c*) and vertical velocity (*d–f*) of a 2D $\Gamma = 1$ cell at $Ra = 10^8$: (*a*,*d* $Pr = 0.045$, (*b*,*e*) $Pr = 0.7$, (*c*,*f*) $Pr = 55$. (*a–c*) Red and blue indicate hot and cold fluid, respectively; (*d–f*) red and blue indicate upward and downward moving fluid, respectively. The temperature colour map is the same for all temperature snapshots in figures 2, 3 and 4 and ranges between $0.4 \leqslant \theta \leqslant 0.6$.

sidewall has to be chosen properly in cylindrical domains. The only way to check this is to perform the same simulations on different resolutions and compare the results (Stevens, Verzicco & Lohse 2010*b*). In order to check this we have performed the simulation for several Prandtl numbers, specifically the lowest and highest, with different resolutions, and we find good agreement between the results obtained at different resolutions. We compared the average length scale in the flow with the largest grid scaling and the time convergence of the results. The results of this analysis are presented in the Appendix.

4. Flow topology

Figures 2, 3 and 4 show flow field snapshots of the complete 2D field, a vertical cross-section and a horizontal cross-section of the 3D cylinder, respectively. The top row (*a–c*) of panels depicts the temperature field and the bottom row (*d–f*) depicts the vertical velocity field. The left (*a*,*d*), centre (*b*,*e*), and right (*c*,*f*) columns are for $Pr = 0.045$, $Pr = 0.7$ and $Pr = 55$, respectively. In the 3D panels it becomes apparent that the temperature structures become more localized at $Pr = 55$, as is

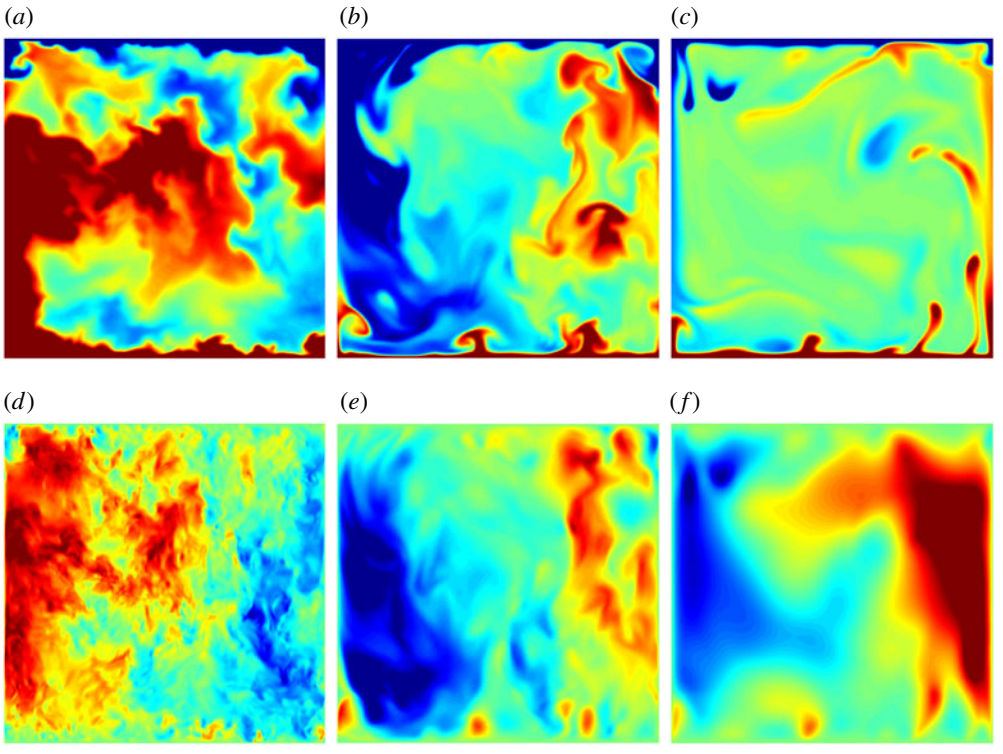

FIGURE 3. Temperature (*a–c*) and vertical velocity (*d–f*) at a vertical plane of a 3D cylindrical $\Gamma = 1$ sample at $Ra = 10^8$: (*a*,*d* $Pr = 0.045$; (*b*,*e*) $Pr = 0.7$; (*c*,*f*) $Pr = 55$. The same colour coding as in figure 2. The azimuthal orientation of these vertical cross-sections can be seen in figure 4.

expected for high Pr flows. At high Pr there is hardly any LSC and the flow is plume-dominated (Verzicco & Camussi 2003). This is reflected in two dimensions, for which the panels of both the temperature and velocity look very similar to those for three dimensions, in agreement with Schmalzl *et al.* (2004), who concluded that the 2D and 3D cases are similar at high Pr due to the vanishing toroidal component of the velocity. Another interpretation of the similarity of the flow topology at high Pr can be made using the plume topology, since at high Pr the flow is plume-dominated. In two dimensions it can be seen that for increasing Pr, the plumes change from the roll-up type to sheet-like and finally to the mushroom type. The roll-up plumes are vortices that become buoyant by extracting thermal energy from the boundary layer. These can be seen in figure 2 for $Pr = 0.045$. The sheet-like plumes are elongated boundary layers stretching upwards and can be found for moderate Pr. For high Pr the flow is dominated by mushroom-shaped plumes. One can imagine that 3D mushroom plumes can be reduced to two dimensions through axisymmetry, while the other types do not possess symmetry that translates from two to three dimensions without violating the divergence-free condition imposed on the velocity field and/or the no-slip boundary conditions. For example, the 3D analogue of a roll-up plume would be a cylinder.

The visual differences emerge at $Pr < 1$. At $Pr = 0.7$ a pronounced LSC with corner rolls in two dimensions can be seen in figure 3. In three dimensions the LSC

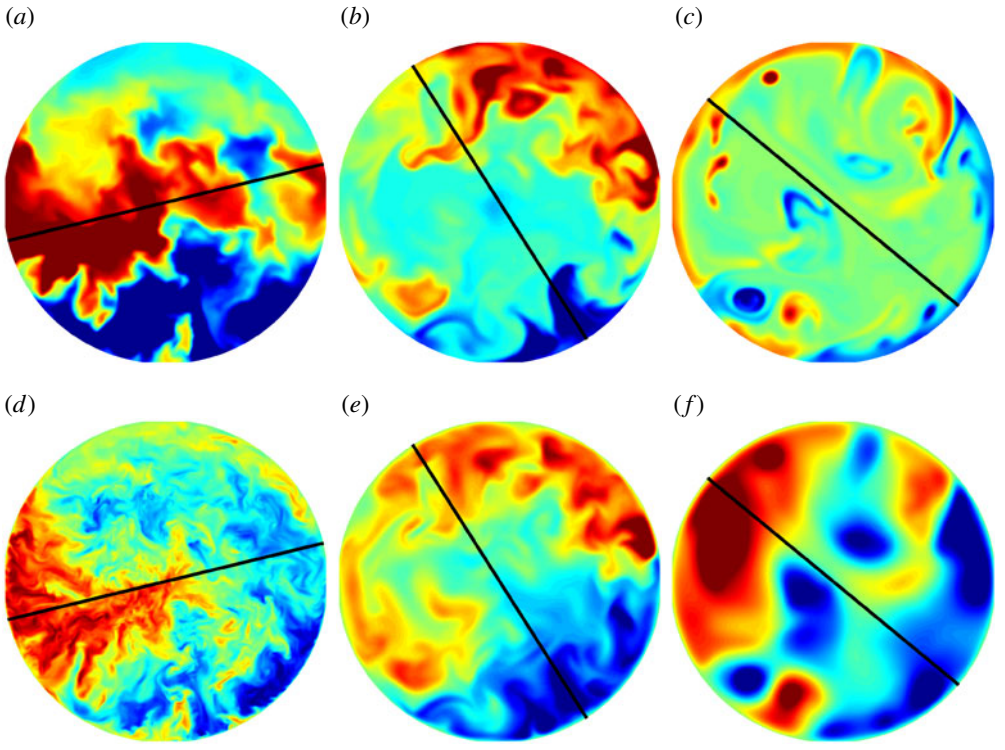

FIGURE 4. Temperature (*a–c*) and vertical velocity (*d–f*) at the horizontal midplane of a $\Gamma = 1$ cell at $Ra = 10^8$: (*a*,*d* $Pr = 0.045$; (*b*,*e*) $Pr = 0.7$; (*c*,*f*) $Pr = 55$. The black lines indicate the azimuthal orientation of the corresponding vertical cross-sections found in figure 3. Note that the velocity scales are visibly smaller than the temperature scales for the small Pr case, while the temperature scales are smaller than the velocity scales for the high Pr case.

is less pronounced and the corner rolls are much smaller. These differences might be due to the absence of a preferential azimuthal orientation of the LSC in three dimensions (Funfschilling & Ahlers 2004; Brown *et al.* 2005; Xi, Zhou & Xia 2006). The azimuthal orientation of the vertical cross-sections displayed here is selected to obtain the clearest depiction of the LSC. In addition, it can be seen that in three dimensions, thermal plumes are emitted from the horizontal centre of the boundary layer and move through the bulk, in contrast to the 2D case. This is because in three dimensions the LSC cannot fully enclose the flow and limit the movement of plumes.

A clear difference between the 2D and 3D cases can be found at $Pr = 0.045$. In particular, the vertical velocity snapshots reveal a drastically different structure. The 2D field has locally very small velocity structures similar to the 3D field. However, even though both the 2D and 3D cases appear to have a large-scale circulation, the average velocity scale in three dimensions is much smaller than in two dimensions. Burr *et al.* (2003) concluded that for $Pr = 0.1$ and $Ra = 10^8$ the LSC is driven by buoyancy forces more than by small-scale turbulent fluctuations in both two and three dimensions. While the small scales do appear to have merged with the LSC in two dimensions, they are possibly not the dominant contribution to the driving of the LSC.

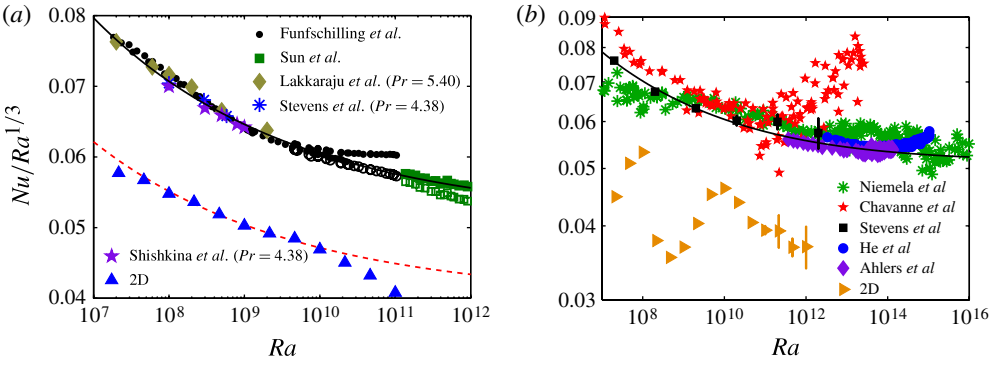

FIGURE 5. (Colour online) (*a*) *Nu* versus *Ra* scaling for water ($Pr = 4.38$) in a $\Gamma = 1$ sample. The simulation result for 2D RB is indicated by the blue upward-pointing triangles. The 3D experimental results from Funfschilling *et al.* (2005) and Sun & Xia (2005) are indicated by circles and squares, respectively. Here the open symbols indicate uncorrected data, while the filled symbols indicate corrected data. The numerical results from Shishkina & Thess (2009), Stevens *et al.* (2011*b*) and Lakkaraju *et al.* (2012) ($Pr = 5.4$) are indicated by the purple stars, blue asterisks and olive diamonds, respectively. The black solid line indicates the GL prediction and the red dashed line indicates the GL prediction multiplied by a constant value A of 0.78. The rest of the points are 3D experimental and numerical data. (*b*) *Nu* versus *Ra* for $Pr = 0.7$ in a $\Gamma = 0.5$ sample. The 2D data are indicated by the yellow rightward-pointing triangles. The stars (Chavanne *et al.* 2001), asterisks (Niemela *et al.* 2000), diamonds (Ahlers *et al.* 2009*a*), circles (He *et al.* 2012; Ahlers *et al.* 2012) indicate experimental data squares indicate results from numerical simulations (Stevens *et al.* 2010*b*; Stevens, Lohse & Verzicco 2011*a*). The refitted GL theory is indicated by the black line.

5. Nusselt number

In this section we will first compare the Rayleigh number scaling of the Nusselt number obtained in 2D and 3D simulations before we compare the Prandtl number dependence in detail.

5.1. *Rayleigh number dependence*

In figure 5(*a*) the compensated Nusselt number $Nu/Ra^{1/3}$ as a function of Ra for $Pr = 4.38$ and $\Gamma = 1$ is displayed. The data are taken from 3D experimental results by Funfschilling *et al.* (2005) and Sun & Xia (2005), 3D numerics by Shishkina & Thess (2009), Stevens *et al.* (2011*b*) and Lakkaraju *et al.* (2012) and the 2D numerics of this research. Both the uncorrected and corrected experimental data are depicted. The corrected data are compensated for finite plate conductivity: see Ahlers *et al.* (2009*b*). In these and forthcoming figures, the 2D data are represented by triangles with varying orientations and the 3D data by other symbols. For reference, the refitted GL prediction for three dimensions is included. Since the 3D data and GL theory display near-equal results for the evaluated Ra range, the latter can be used as a guide to comparing the 2D $Nu(Ra)$ data with 3D data by rescaling with a constant factor of 0.78. For two and three dimensions the scaling of $Nu(Ra)$ agrees very well for $10^7 \leqslant Ra \leqslant 10^{10}$. At higher Ra the 2D points are smaller than the rescaled 3D GL prediction. This indicates that for $Ra > 10^{10}$ the 2D scaling differs from the 3D scaling since the 3D data do follow this scaling. An analysis of the roll states of $Ra = 4.64 \times 10^9$ and $Ra = 10^{10}$ reveals that there is a substantial change in flow state between these Rayleigh numbers, which might be connected to the

discrepancy in scaling. At $Ra = 4.64 \times 10^9$, the flow is in a single roll state similar to the state depicted for $Pr = 0.7$ and $Ra = 10^8$ in figure 2, while at $Ra = 10^{10}$ the roll state has become uncondensed. Here, the term uncondensed signifies that there is no energy pile-up at a scale close to system size and thus there is no LSC. The largest scale in the flow consists of two mobile and orbiting smaller rolls. That *Nu* is (counter-intuitively) lower for this broken LSC has been observed previously by van der Poel *et al.* (2012) for $Pr = 0.7$ and $Ra = 10^9$, and we believe that this is due to the increased path length of the thermal plumes before they can deliver the heat to the opposite plate. For a large-scale circulation the plumes move directly from their original boundary layer to the opposite boundary layer, while otherwise the plumes move less directly to the opposite boundary layer, interacting with the multiple rolls composing the bulk. Now, not only the absolute *Nu* but also the scaling between *Nu* and *Ra* appears to be lower for this roll state. Extrapolating towards higher *Ra*, one expects that the scaling will change subsequently when these orbiting rolls are replaced by a more complex roll state with even smaller scales. Eventually, the fluctuations will become too large and the scales too small for the existence of a coherent roll state that can affect integral quantities. In van der Poel *et al.* (2012) we showed that the scaling of Nusselt can change locally in 2D RB convection and can recover to the expected 3D scaling for higher *Ra*; see also the $\Gamma = 1/2$ results.

In three dimensions no such transition in an integral quantity exists, since the LSC does not fully enclose the system. This gives the thermal plumes more freedom to move from one boundary layer to another. Therefore, the difference in *Nu* between a system with a single roll state and one with a broken single roll state is expected to be small and more gradual than in two dimensions, where the system can jump between these states, affecting *Nu* (van der Poel *et al.* 2012) and its scaling.

The difference between the 2D and 3D cases is expected to be larger for lower *Pr* due to the larger toroidal component of the velocity. In addition, it is known from van der Poel *et al.* (2011) that the integral quantities and flow state in two dimensions have a stronger dependence on the aspect ratio Γ than in three dimensions (Bailon-Cuba, Emran & Schumacher 2010). This is emphasized by the increased effect of the flow state on *Nu* for low *Pr* due to the thermal boundary layer being exposed to the bulk flow (van der Poel *et al.* 2011). For low *Pr*, the bulk flow directly extracts heat from the thermal boundary layer, and therefore the flow state of the bulk has a large effect on *Nu*. We therefore include a comparison for $Pr = 0.7$ and $\Gamma = 0.5$, where we expect a substantial difference. The result is displayed in figure 5(*b*). Although the average scaling exponent appears to be similar, the 2D data reveal much more structure than for three dimensions. This is caused by multi-stability of different flow states and the large difference in *Nu* between these flow states. By increasing *Ra*, the system is successively in a triple roll state, an unstable triple roll state and back to a triple roll state, passing through an unstable region until the roll state breaks up. These roll states strongly affect the resulting *Nu*. This effect is expected to decrease as the LSC loses its strength (van der Poel *et al.* 2012) and the length scales become smaller at higher *Ra*.

5.2. *Prandtl number dependence*

The main conclusion from Schmalzl *et al.* (2004) was that the agreement of global quantities between two and three dimensions depends on *Pr*. More specifically, they conclude that for lower *Pr* the 2D output increasingly deviates from the 3D output. We repeat their measurements in two dimensions for $Ra = 10^6$ and supplement them with a series for $Ra = 10^8$, albeit with a no-slip boundary condition on the sidewalls

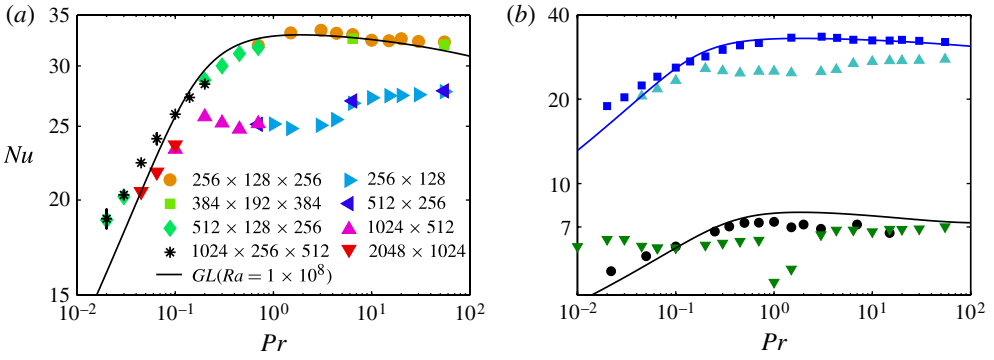

FIGURE 6. (Colour online) Nu as function of Pr. (a) The Nusselt number obtained in numerical simulation performed on different grids for $Ra = 10^8$. The legend indicates the number of gridpoints in the vertical and horizontal direction for two dimensions and in the azimuthal, radial, and axial direction for three dimensions. (b) Comparison of the Pr number dependence on Nu in two and three dimensions. Here the green downward-pointing and cyan upward-pointing triangles indicate the results from 2D RB simulations at $Ra = 10^8$ and $Ra = 10^6$, respectively. For three dimensions this is indicated by the blue squares and black circles, respectively. The $Ra = 10^6$ data are from Verzicco & Camussi (1999). In both panels the solid lines give the prediction of the GL theory.

in contrast to their stress-free sidewall boundary condition. In figure 6(a) it can be seen that numerical simulations for low Pr become increasingly demanding in terms of resolution. Here the results for the $Ra = 10^8$ runs are depicted, with symbols indicating the numerical resolution used. Figure 6(b) shows $Nu(Pr)$ for Ra for 10^6 and 10^8. The solid lines are the refitted theoretical GL predictions for the different Ra corresponding to the experimental and numerical data. First, we observe that the numerical results for 2D (green triangles) and 3D (black dots) at $Ra = 10^6$ display no qualitative similarity, except for the Pr independence of Nu at higher Pr. Furthermore, in two dimensions multiple states are observed around $Pr = 1$, where the outlying points are caused by the double roll state of the system as opposed to the single roll state corresponding to the other data points. It is likely that the single roll state is stable as well, which would display a Nu similar to the surrounding Pr data (van der Poel *et al.* 2011). However, this has not been checked. The discrepancy that Schmalzl *et al.* (2004) did not observe these multiple states might be due to multi-stability or caused by their free-slip sidewall boundary condition. For $Ra = 10^8$ the 2D and 3D cases seem to converge for high Pr. The largest difference is seen at intermediate Pr, which is reflected in the flow topology: see § 4. Here the strong LSC results in a substantial difference in Nu between the 2D and 3D cases. At low Pr, unlike for $Ra = 10^6$, the 2D and 3D Nu are matching. However, the number of data points is too low to make a strong conclusion given this surprising low Pr behaviour.

6. Reynolds number

Figure 7 shows the comparison for the compensated Reynolds number based on the r.m.s. vertical velocity $Re_3^{RMS} = u_3^{RMS}L/\nu$ as a function of both Ra and Pr. The data in figure 7(a) correspond to the low $Pr = 0.7$ and low $\Gamma = 0.5$ parameters, where we expect a large difference. This is confirmed for Nu in figure 5(b) and appears to be the same for Re_3^{RMS}. A similar difference in structure between the 2D and 3D cases

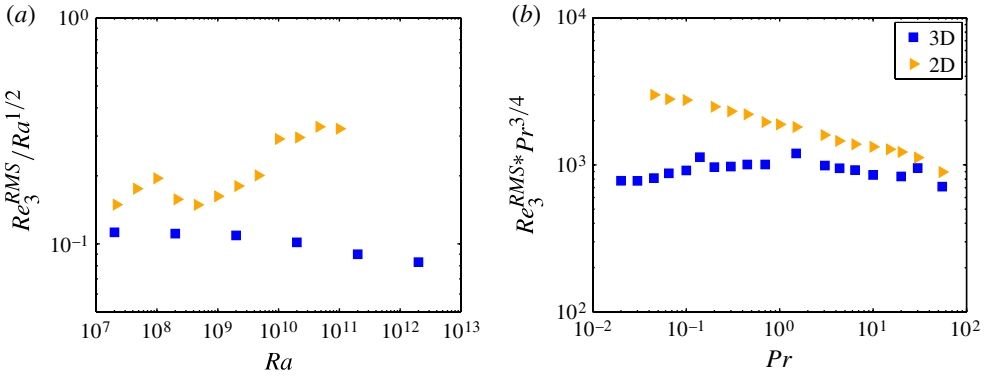

FIGURE 7. (Colour online) The compensated Reynolds number based on the r.m.s. vertical velocity Re_3^{RMS} for 2D (rightward-pointing triangles) and 3D (squares): (*a*) Re_3^{RMS} as a function of Ra for $Pr = 0.7$ and $\Gamma = 0.5$; (*b*) Re_3^{RMS} as a function of Pr for $Ra = 10^8$ and $\Gamma = 1$. The legend in (*b*) applies to both plots. Corresponding Nu comparison can be found in figures 5(*b*) and 6(*b*) for (*a*) and (*b*), respectively.

can be seen, with no noticeable convergence at the highest Ra evaluated. Re_3^{RMS} can be seen locally to scale larger than $Ra^{1/2}$ for two dimensions, which highlights the roll state dependence of integral quantities in two dimensions. The comparison of Re_3^{RMS} as a function of Pr in figure 7(*b*) reveals a picture similar to that seen by Schmalzl *et al.* (2004) for $Ra = 10^6$: the Reynolds number for two dimensions converges to the 3D value at high Pr. In both cases the 2D Re_3^{RMS} is higher than in three dimensions, while in contrast Nu is lower in two dimensions compared to three dimensions. The inverse energy cascade in two dimensions is possibly causing a stronger LSC than in three dimensions. However, up to now there have been no studies of the existence of the inverse energy cascade in 2D RB, and therefore this remains uncertain. It could also be that in two dimensions all emitted plumes drive the LSC, while in three dimensions not all plumes follow the motion of the LSC. This can result in a lower Nu due to plumes being dragged down by the LSC before releasing most of their thermal energy at the boundary opposite to the plumes' origin. In this situation Re_3^{RMS} can be higher in two dimensions while Nu is lower.

7. Boundary layer profile

The boundary layer profile is a fundamental ingredient in most theoretical studies of the scaling of Nu and Re. In the 'classical' regime, where the boundary layer is assumed to be laminar, a reference analytical solution for the situation of a flow over a infinitely long plate is provided by Pohlhausen (1921), which is based on the Prandtl–Blasius (PB) boundary layer approximation. The purpose of this section is to compare the 2D and 3D boundary layer profiles, with the Pohlhausen profile included for reference. For a laminar boundary layer, it is assumed that for $Pr \approx 1$ both the velocity and temperature have a similar profile. This allows us to use the temperature boundary layer profile that is relatively easy to extract, for comparison. It is known that the time-averaged and instantaneous laminar boundary layers at the centre of a large-scale roll in both 2D and 3D RB flow are well approximated by the Pohlhausen profile when dynamically rescaled (Zhou & Xia 2010; Zhou *et al.* 2010; Stevens *et al.* 2012). This is despite the fact that the instantaneous flow in RB is only in rare cases

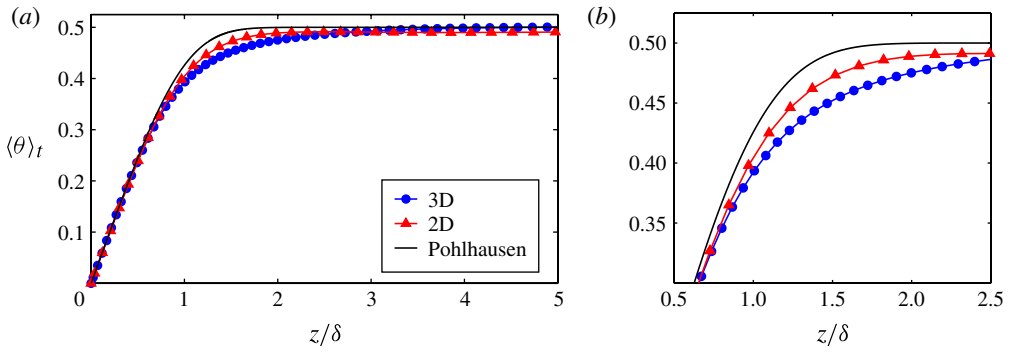

FIGURE 8. (Colour online) (*a*) Thermal boundary layer profile for two dimensions (red triangles) and three dimensions (blue dots) compared to the Pohlhausen solution (black line) of the Prandtl–Blasius laminar boundary layer approximation. The 2D and 3D cases used for the profiles have identical $Pr = 4.38$ and Ra is varied to obtain an approximately equal Nu. For three dimensions $Ra = 10^8$ and $Nu = 33.11$ and for two dimensions $Ra = 2.25 \times 10^8$ and $Nu = 33.26$. (*b*) A close-up of (*a*).

locally parallel to the plates, in contrast to the PB assumptions of a completely parallel flow. The resulting deviations have been studied in detail for several cases (Wagner, Shishkina & Wagner 2012; Shi, Emran & Schumacher 2012; Scheel, Kim & White 2012). The vertical velocity gradient is non-zero due to the LSC, plume emission and corner rolls. As this effect is minimal at the centre of a roll for most control parameters, the temperature profile is measured in the centre of the cell: $r = 0$ for 3D and $x = D/2$ for 2D in a $\Gamma = 1$ cell. It was shown by Zhou *et al.* (2010) that the lateral dependence is strong. In figure 8 the time-averaged temperature profiles for two and three dimensions for identical $Pr = 4.38$ and the Pohlhausen solution are shown. The Ra number is varied to match Nu in two and three dimensions to obtain an equal temperature boundary layer thickness $\lambda_\theta \approx 1/(2Nu)$ and similar local flow conditions induced by the heat flux. The profiles are measured in the laboratory frame in order to reveal the differences, as both the 2D and 3D profiles match the Pohlhausen profile when measured in the dynamical frame.

It can be seen that neither the 2D and 3D profiles in figure 8 match the Pohlhausen profile well in the laboratory frame. The agreement of the 3D profile is worse than that of the 2D profile. This is most likely due to a combination of several causes. The PB theory is a 2D theory and, because of the more complex dynamics of the LSC in three dimensions compared with two dimensions, the velocity field cannot be considered to be constantly parallel to the horizontal plates, even at $r = 0$. Furthermore, increased plume activity in the bulk indicates that more plumes are emitted at the centre of the 3D cell due to the increased degrees of freedom and LSC cessations. This results in the 3D profile being lower than 2D throughout the boundary layer, as an increased amount of thermal energy is taken by plumes.

8. Conclusion

The comparability of 2D and 3D Rayleigh–Bénard convection can in most cases be explained using the coherent structures present in the flow. At high Pr, the regime dominated by mushroom-type plumes, similar 2D and 3D behaviour is observed, as expected. However, the LSC in two dimensions has a largely different effect on heat

transport compared to three dimensions. In two dimensions the LSC covers the full system, causing the plume movement to be dominated by the LSC, resulting in a significant discrepancy in this regime. The Ra and Pr scaling of the integral quantities in two and three dimensions are similar in some parameter regions. For $Ra = 10^8$, Nu appears similar for low and high Pr while it is substantially different for $Pr \approx 1$. The similarity at low Pr is surprising, as Schmalzl *et al.* (2004) concluded, albeit for $Ra = 10^6$, that here the 2D and 3D cases become incomparable. For $Pr = 4.3$ the $Nu(Ra)$ scaling is nearly identical, with only a constant factor between them up to $Ra = 10^{10}$. The temperature boundary layer profiles of both two and three dimensions, obtained in the laboratory frame, differ from the Pohlhausen profile and from each other. As expected, the 2D boundary layer is closer to the Pohlhausen profile.

It is not difficult to find parameters for which there is a large difference between two and three dimensions. At low aspect ratios the flow states in two dimensions vary more strongly than in three dimensions and have a larger effect on Nu and Re, in particular for $Pr < 1$ (van der Poel *et al.* 2011). This is reflected in the $Nu(Ra)$ analysis at $\Gamma = 0.5$, where the 3D scaling is smooth and the 2D scaling is very structured. Less expected is the deviation at $Pr = 4.3$ for $Ra > 10^{10}$, which concurs with a change in flow state in two dimensions. At this Ra the LSC breaks up, and one would expect more similarity since the 3D LSC differs strongly from the 2D LSC in that it does not limit the movement of plumes as much. Adding to the question is the discrepancy in $Nu(Ra)$ around $Pr = 1$. Here, the flow state is a large-scale circulation resulting in decreased similarity, in contrast to the increased similarity in the $Nu(Ra)$ scaling.

A remarkable difference is found for Re_3^{RMS}, which is in contrast to Nu, higher in two dimensions than in three. This can be attributed to the strong LSC in two dimensions, dragging thermal plumes back towards their originating plates before they can release their thermal energy.

Acknowledgements

The authors acknowledge useful discussions with R. Verzicco and S. Grossmann. This study is supported by FOM and the National Computing Facilities (NCF), both sponsored by NWO. This work was granted access to the HPC resources of SARA made available within the Distributed European Computing Initiative by the PRACE-2IP, receiving funding from the European Community's Seventh Framework Programme (FP7/2007-2013) under grant agreement RI-283493.

Appendix. Details of numerical simulations

Tables 1 and 2 summarize the details of the 3D and 2D simulations that are presented in this study. The data are presented in a similar way to table 1 of Stevens *et al.* (2010*b*). The tables indicate the grid resolution used for the different Pr number cases and compare the resolution used in the boundary layer with the criterion given in equation (42) of Shishkina *et al.* (2010). The resolution over the whole domain is compared by using (2.5) and (2.6) of Stevens *et al.* (2010*b*) and using $h = \max(\Delta x, \Delta y, \Delta z)$ or $h = \max(\Delta r, \Gamma L/2\Delta\phi, \Delta z)$ in a cylindrical domain. Note that for high Pr number regime (2.6) of Stevens *et al.* (2010*b*) is more restrictive than the criterion given in (37) of Shishkina *et al.* (2010). The current results seem to indicate that the criterion of Shishkina *et al.* (2010) is sufficient to ensure convergence of the Nusselt number for the high Pr number cases.

Pr	$N_\theta \times N_r \times N_z$	N_{BL}	N_{BL}^{min}	h	Nu_f	Nu_h	τ_f	Ref.
55.00	**384 × 192 × 384**	**15**	**8**	**1.68**	**32.00**	**32.00**	**600**	Stevens *et al.* (2010*a*)
55.00	256 × 128 × 256	23	8	2.52	32.25	32.20	750	Stevens *et al.* (2010*a*)
30.00	256 × 128 × 256	15	8	2.17	32.31	32.40	600	Stevens *et al.* (2010*a*)
20.00	256 × 128 × 256	15	8	1.97	32.54	32.56	400	Stevens *et al.* (2010*a*)
15.00	256 × 128 × 256	15	8	1.83	32.36	32.60	400	Zhong *et al.* (2009)
10.00	256 × 128 × 256	15	8	1.65	32.42	32.53	400	Zhong *et al.* (2009)
6.400	**384 × 192 × 384**	**23**	**8**	**0.99**	**32.59**	**32.42**	**400**	Stevens *et al.* (2010*a*)
6.400	256 × 128 × 256	15	8	1.48	32.95	33.00	200	Zhong *et al.* (2009)
4.380	256 × 128 × 256	15	8	1.35	33.15	32.91	400	Zhong *et al.* (2009)
3.050	256 × 128 × 256	15	8	1.24	33.48	33.45	400	Zhong *et al.* (2009)
1.500	256 × 128 × 256	15	8	1.03	33.13	33.13	400	Zhong *et al.* (2009)
0.700	**512 × 128 × 256**	**12**	**9**	**0.58**	**31.71**	**31.79**	**302**	This work
0.700	256 × 128 × 256	15	9	1.11	31.94	31.88	400	Zhong *et al.* (2009)
0.450	512 × 128 × 256	12	12	0.73	31.13	31.22	259	This work
0.300	512 × 128 × 256	13	15	0.88	30.00	30.03	341	This work
0.200	**1024 × 256 × 512**	**27**	**18**	**0.53**	**28.40**	**28.64**	**151**	This work
0.200	512 × 128 × 256	13	18	1.07	28.73	28.68	377	This work
0.140	1024 × 256 × 512	28	22	0.63	27.27	27.37	135	This work
0.100	1024 × 256 × 512	29	27	0.74	25.93	25.84	123	This work
0.065	1024 × 256 × 512	30	35	0.90	24.07	23.64	126	This work
0.045	1024 × 256 × 512	33	45	1.05	22.38	22.26	100	This work
0.030	**1024 × 256 × 512**	**39**	**57**	**1.35**	**20.31**	**20.04**	**56**	This work
0.030	512 × 128 × 256	18	57	2.55	20.20	20.48	447	This work
0.020	**1024 × 256 × 512**	**44**	**76**	**1.61**	**18.90**	**19.46**	**78**	This work
0.020	512 × 128 × 256	19	76	3.04	18.82	18.59	414	This work

TABLE 1. Details of 3D simulations at $Ra = 10^8$. Columns from left to right: Pr number; resolution in azimuthal, radial and axial direction, $N_\theta \times N_r \times N_z$; number of points in the thermal boundary layer used in the simulation; minimum number of points that should be used in the thermal boundary layer according to Shishkina *et al.* (2010); average length scale in the flow compared to the largest grid length used in the grid, h; Nu_f, the Nusselt number over the whole simulation length, omitting the initialization period; Nu_h, the Nusselt number over the last half of the simulation time considered; τ_f, the simulation time in free-fall time units after the initialization period of 30 to $200\tau_f$ considered; reference where the simulation was first presented. Bold type indicates Pr numbers for which the effect of the numerical resolution has been tested.

In table 1 it can be seen that for some of the low Pr number cases the boundary layers are under-resolved according to the Shishkina *et al.* (2010) criterion. However, the agreement of Nu for identical parameters and different grid resolutions indicate that at least for integral quantities the resolution is sufficient and that the criterion is possibly too strict for low Pr. We also note that here the minimum number of grid points is determined using the new $a = 0.911$ (Stevens *et al.* 2013), while numerical tests (Shishkina *et al.* 2010) indicate that the minimum number of gridpoints required in the boundary layer is closer to the value obtained by using the old $a = 0.482$.

Pr	$N_x \times N_y$	N_{BL}	N_{BL}^{min}	h	Nu_f	Nu_h	τ_f
55.00	**512 × 256**	**16**	**7**	**1.27**	**27.83**	**27.86**	**50000**
55.00	256 × 128	8	7	2.38	27.76	27.75	50000
30.00	256 × 128	8	7	2.38	27.50	27.51	40000
20.00	256 × 128	8	7	2.38	27.44	27.44	30000
10.00	256 × 128	8	7	2.37	27.25	27.26	20000
6.400	**512 × 256**	**16**	**7**	**1.26**	**26.99**	**26.99**	**10000**
6.400	256 × 128	8	7	2.36	26.79	26.79	20000
4.380	256 × 128	8	7	2.33	25.51	25.47	30000
3.000	256 × 128	8	7	2.32	25.07	25.05	10000
1.500	256 × 128	8	7	2.31	24.83	24.82	10000
1.000	512 × 256	8	7	2.32	25.17	25.16	10000
0.700	**1024 × 512**	**30**	**8**	**0.78**	**25.22**	**25.10**	**8000**
0.700	512 × 256	15	8	1.48	25.14	25.16	8000
0.450	1024 × 512	34	11	0.96	24.78	24.59	2000
0.300	1024 × 512	37	13	1.18	25.25	25.09	2000
0.200	1024 × 512	34	17	1.43	25.73	25.40	1500
0.100	**2048 × 1024**	**76**	**26**	**1.01**	**23.63**	**23.18**	**200**
0.100	1024 × 512	36	26	1.97	23.32	23.03	1000
0.065	2048×1024	82	34	1.23	21.76	22.07	200
0.045	2048×1024	102	43	1.46	20.52	20.95	80

TABLE 2. Details of 2D simulations at $Ra = 10^8$. Columns from left to right: Pr number; resolution in horizontal and vertical direction, $N_x \times N_y$; number of points in the thermal boundary layer used in the simulation; minimum number of points that should be used in the thermal boundary layer according to Shishkina *et al.* (2010); average length scale in the flow compared to the largest grid length used in the grid, h; τ_f, the simulation time in free-fall time units after the initialization period of 30 to $3000\tau_f$ considered. Bold type indicates Pr numbers for which the effect of the numerical resolution has been tested.

REFERENCES

AHLERS, G., BODENSCHATZ, E., FUNFSCHILLING, D. & HOGG, J. 2009*a* Turbulent Rayleigh–Bénard convection for a Prandtl number of 0.67. *J. Fluid. Mech.* **641**, 157–167.

AHLERS, G., GROSSMANN, S. & LOHSE, D. 2009*b* Heat transfer and large-scale dynamics in turbulent Rayleigh–Bénard convection. *Rev. Mod. Phys.* **81**, 503.

AHLERS, G., HE, X., FUNFSCHILLING, D. & BODENSCHATZ, E. 2012 Heat transport by turbulent Rayleigh–Bénard convection for $Pr = 0.8$ and $3 \times 10^{12} \lesssim Ra \lesssim 10^{15}$: aspect ratio $\Gamma = 0.50$. *New J. Phys.* **14**, 103012.

BAILON-CUBA, J., EMRAN, M. S. & SCHUMACHER, J. 2010 Aspect ratio dependence of heat transfer and large-scale flow in turbulent convection. *J. Fluid Mech.* **655**, 152–173.

BROWN, E., FUNFSCHILLING, D., NIKOLAENKO, A. & AHLERS, G. 2005 Heat transport in turbulent Rayleigh–Bénard convection: effect of finite top- and bottom-plate conductivities. *Phys. Fluids* **17**, 075108.

BURR, U., KINZELBACH, W. & TSINOBER, A. 2003 Is the turbulent wind in convective flows driven by fluctuations? *Phys. Fluids* **15**, 2313–2320.

BUSSE, F. H. 1978 Non-linear properties of thermal convection. *Rep. Prog. Phys.* **41**, 1929–1967.

CASTAING, B., GUNARATNE, G., HESLOT, F., KADANOFF, L., LIBCHABER, A., THOMAE, S., WU, X. Z., ZALESKI, S. & ZANETTI, G. 1989 Scaling of hard thermal turbulence in Rayleigh–Bénard convection. *J. Fluid Mech.* **204**, 1–30.

CHANDRA, M. & VERMA, M. K. 2011 Dynamics and symmetries of flow reversals in turbulent convection. *Phys. Rev.* E **83**, 067303.

CHAUMAT, S., CASTAING, B. & CHILLA, F. 2002 Rayleigh–Bénard cells: influence of plate properties. In *Advances in Turbulence IX* (ed. I. P. Castro, P. E. Hancock & T. G. Thomas), International Center for Numerical Methods in Engineering, CIMNE.

CHAVANNE, X., CHILLA, F., CHABAUD, B., CASTAING, B. & HEBRAL, B. 2001 Turbulent Rayleigh–Bénard convection in gaseous and liquid He. *Phys. Fluids* **13**, 1300–1320.

DELUCA, E. E., WERNE, J., ROSNER, R. & CATTANEO, F. 1990 Numerical simulations of soft and hard turbulence: preliminary results for two-dimensional convection. *Phys. Rev. Lett.* **64**, 2370–2373.

FLEISCHER, A. S. & GOLDSTEIN, R. J. 2002 High-Rayleigh-number convection of pressurized gases in a horizontal enclosure. *J. Fluid Mech.* **469**, 1–12.

FUNFSCHILLING, D. & AHLERS, G. 2004 Plume motion and large-scale circulation in a cylindrical Rayleigh–Bénard cell. *Phys. Rev. Lett.* **92**, 194502.

FUNFSCHILLING, D., BROWN, E., NIKOLAENKO, A. & AHLERS, G. 2005 Heat transport by turbulent Rayleigh–Bénard convection in cylindrical cells with aspect ratio one and larger. *J. Fluid Mech.* **536**, 145–154.

GROSSMANN, S. & LOHSE, D. 2000 Scaling in thermal convection: a unifying view. *J. Fluid. Mech.* **407**, 27–56.

GROSSMANN, S. & LOHSE, D. 2001 Thermal convection for large Prandtl number. *Phys. Rev. Lett.* **86**, 3316–3319.

GROSSMANN, S. & LOHSE, D. 2002 Prandtl and Rayleigh number dependence of the Reynolds number in turbulent thermal convection. *Phys. Rev.* E **66**, 016305.

GROSSMANN, S. & LOHSE, D. 2004 Fluctuations in turbulent Rayleigh–Bénard convection: the role of plumes. *Phys. Fluids* **16**, 4462–4472.

GROSSMANN, S. & LOHSE, D. 2011 Multiple scaling in the ultimate regime of thermal convection. *Phys. Fluids* **23**, 045108.

HE, X., FUNFSCHILLING, D., NOBACH, H., BODENSCHATZ, E. & AHLERS, G. 2012 Transition to the ultimate state of turbulent Rayleigh–Bénard convection. *Phys. Rev. Lett* **108**, 024502.

JOHNSTON, H. & DOERING, C. R. 2009 Comparison of turbulent thermal convection between conditions of constant temperature and constant flux. *Phys. Rev. Lett.* **102**, 064501.

KRAICHNAN, R. 1967 Inertial ranges in two-dimensional turbulence. *Phys. Fluids* **10**, 1417.

LAKKARAJU, R., STEVENS, R. J. A. M., VERZICCO, R., GROSSMANN, S., PROSPERETTI, A., SUN, C. & LOHSE, D. 2012 Spatial distribution of heat flux and fluctuations in turbulent Rayleigh–Bénard convection. *Phys. Rev.* E **86**, 056315.

NIEMELA, J., SKRBEK, L., SREENIVASAN, K. R. & DONNELLY, R. 2000 Turbulent convection at very high Rayleigh numbers. *Nature* **404**, 837–840.

VAN DER POEL, E. P., STEVENS, R. J. A. M. & LOHSE, D. 2011 Connecting flow structures and heat flux in turbulent Rayleigh–Bénard convection. *Phys. Rev.* E **84**, 045303(R).

VAN DER POEL, E. P., STEVENS, R. J. A. M., SUGIYAMA, K. & LOHSE, D. 2012 Flow states in two-dimensional Rayleigh–Bénard convection as a function of aspect-ratio and Rayleigh number. *Phys. Fluids* **24**, 085104.

POHLHAUSEN, K. 1921 Zur nährungsweisen Integration der Differentialgleichung der laminaren Grenzschicht. *Z. Angew. Math. Mech.* **1**, 252–268.

ROBERTS, G. O. 1979 Fast viscous Bénard convection. *Geophys. Astrophys. Fluid Dyn.* **12**, 235–272.

ROCHE, P.-E., GAUTHIER, F., KAISER, R. & SALORT, J. 2010 On the triggering of the ultimate regime of convection. *New J. Phys.* **12**, 085014.

SCHEEL, J., KIM, E. & WHITE, K. 2012 Thermal and viscous boundary layers in turbulent Rayleigh–Bénard convection. *J. Fluid. Mech.* **711**, 281–305.

SCHMALZL, J., BREUER, M., WESSLING, S. & HANSEN, U. 2004 On the validity of two-dimensional numerical approaches to time-dependent thermal convection. *Europhys. Lett.* **67**, 390–396.

SHI, N., EMRAN, M. & SCHUMACHER, J. 2012 Boundary layer structure in turbulent Rayleigh–Bénard convection. *J. Fluid. Mech.* **706**, 5–33.

SHISHKINA, O., STEVENS, R. J. A. M., GROSSMANN, S. & LOHSE, D. 2010 Boundary layer structure in turbulent thermal convection and its consequences for the required numerical resolution. *New J. Phys.* **12**, 075022.

SHISHKINA, O. & THESS, A. 2009 Mean temperature profiles in turbulent Rayleigh–Bénard convection of water. *J. Fluid Mech.* **633**, 449–460.

SHRAIMAN, B. I. & SIGGIA, E. D. 1990 Heat transport in high-Rayleigh number convection. *Phys. Rev.* A **42**, 3650–3653.

STEVENS, R. J. A. M., VAN DER POEL, E. P., GROSSMANN, S. & LOHSE, D. 2013 The unifying theory of scaling in thermal convection: the updated prefactors. *J. Fluid. Mech.* **730**, 295–308.

STEVENS, R. J. A. M., ZHOU, Q., GROSSMANN, S., VERZICCO, R., XIA, K.-Q. & LOHSE, D. 2012 Thermal boundary layer profiles in turbulent Rayleigh–Bénard convection in a cylindrical sample. *Phys. Rev.* E **85**, 027301.

STEVENS, R. J. A. M., CLERCX, H. J. H. & LOHSE, D. 2010*a* Optimal Prandtl number for heat transfer in rotating Rayleigh–Bénard convection. *New J. Phys.* **12**, 075005.

STEVENS, R. J. A. M., LOHSE, D. & VERZICCO, R. 2011*a* Prandtl number dependence of heat transport in high Rayleigh number thermal convection. *J. Fluid. Mech.* **688**, 31–43.

STEVENS, R. J. A. M., OVERKAMP, J., LOHSE, D. & CLERCX, H. J. H. 2011*b* Effect of aspect-ratio on vortex distribution and heat transfer in rotating Rayleigh–Bénard. *Phys. Rev.* E **84**, 056313.

STEVENS, R. J. A. M., VERZICCO, R. & LOHSE, D. 2010*b* Radial boundary layer structure and Nusselt number in Rayleigh–Bénard convection. *J. Fluid. Mech.* **643**, 495–507.

SUGIYAMA, K., CALZAVARINI, E., GROSSMANN, S. & LOHSE, D. 2007 Non-Oberbeck–Boussinesq effects in Rayleigh–Bénard convection: beyond boundary-layer theory. *Europhys. Lett.* **80**, 34002.

SUGIYAMA, K., CALZAVARINI, E., GROSSMANN, S. & LOHSE, D. 2009 Flow organization in two-dimensional non-Oberbeck–Boussinesq Rayleigh–Bénard convection in water. *J. Fluid Mech.* **637**, 105–135.

SUGIYAMA, K., NI, R., STEVENS, R. J. A. M., CHAN, T. S., ZHOU, S.-Q., XI, H.-D., SUN, C., GROSSMANN, S., XIA, K.-Q. & LOHSE, D. 2010 Flow reversals in thermally driven turbulence. *Phys. Rev. Lett.* **105**, 034503.

SUN, C. & XIA, K.-Q. 2005 Scaling of the Reynolds number in turbulent thermal convection. *Phys. Rev.* E **72**, 067302.

URBAN, P., HANZELKA, P., KRALIK, T., MUSILOVA, V., SRNKA, A. & SKRBEK, L. 2012 Effect of boundary layers asymmetry on heat transfer efficiency in turbulent Rayleigh–Bénard convection at very high Rayleigh numbers. *Phys. Rev. Lett.* **109**, 154301.

URBAN, P., MUSILOVÁ, V. & SKRBEK, L. 2011 Efficiency of heat transfer in turbulent Rayleigh–Bénard convection. *Phys. Rev. Lett.* **107**, 014302.

VERZICCO, R. & CAMUSSI, R. 1999 Prandtl number effects in convective turbulence. *J. Fluid Mech.* **383**, 55–73.

VERZICCO, R. & CAMUSSI, R. 2003 Numerical experiments on strongly turbulent thermal convection in a slender cylindrical cell. *J. Fluid Mech.* **477**, 19–49.

VERZICCO, R. & ORLANDI, P. 1996 A finite-difference scheme for three-dimensional incompressible flow in cylindrical coordinates. *J. Comput. Phys.* **123**, 402–413.

VINCENT, A. P. & YUEN, D. A. 2000 Transition to turbulent thermal convection beyond $Ra = 10^{10}$ detected in numerical simulations. *Phys. Rev.* E **61**, 5241.

WAGNER, S., SHISHKINA, O. & WAGNER, C. 2012 Boundary layers and wind in cylindrical Rayleigh–Bénard cells. *J. Fluid. Mech.* **697**, 336–366.

WEISS, S., STEVENS, R. J. A. M., ZHONG, J.-Q., CLERCX, H. J. H., LOHSE, D. & AHLERS, G. 2010 Finite-size effects lead to supercritical bifurcations in turbulent rotating Rayleigh–Bénard convection. *Phys. Rev. Lett.* **105**, 224501.

WERNE, J. 1993 Structure of hard-turbulent convection in two-dimensions: numerical evidence. *Phys. Rev.* E **48**, 1020–1035.

WERNE, J., DELUCA, E. E., ROSNER, R. & CATTANEO, F. 1991 Development of hard-turbulence convection in two dimensions: numerical evidence. *Phys. Rev. Lett.* **67**, 3519.

XI, H.-D., ZHOU, Q. & XIA, K.-Q. 2006 Azimuthal motion of the mean wind in turbulent thermal convection. *Phys. Rev.* E **73**, 056312.

ZHONG, J.-Q., STEVENS, R. J. A. M., CLERCX, H. J. H., VERZICCO, R., LOHSE, D. & AHLERS, G. 2009 Prandtl-, Rayleigh-, and Rossby-number dependence of heat transport in turbulent rotating Rayleigh–Bénard convection. *Phys. Rev. Lett.* **102**, 044502.

ZHOU, Q., STEVENS, R. J. A. M., SUGIYAMA, K., GROSSMANN, S., LOHSE, D. & XIA, K.-Q. 2010 Prandtl–Blasius temperature and velocity boundary layer profiles in turbulent Rayleigh–Bénard convection. *J. Fluid. Mech.* **664**, 297–312.

ZHOU, Q. & XIA, K.-Q. 2010 Measured instantaneous viscous boundary layer in turbulent Rayleigh–Bénard convection. *Phys. Rev. Lett.* **104**, 104301.